Title
Microcalcification detectability using a bench-top prototype photon-counting breast CT based on a Si strip detector

Journal
Medical Physics, 42(7)

ISSN
0094-2405

Authors
Cho, Hyo-Min
Ding, Huanjun
Barber, William C
et al.

Publication Date
2015-06-29

DOI
10.1118/1.4922680

Microcalcification detectability using a bench-top prototype photon-counting breast CT based on a Si strip detector

Hyo-Min Cho[a] and Huanjun Ding
Department of Radiological Sciences, University of California, Irvine, California 92697

William C. Barber and Jan S. Iwanczyk
DxRay Inc., Northridge, California 91324

Sabee Molloi[b]
Department of Radiological Sciences, University of California, Irvine, California 92697

(Received 18 December 2014; revised 12 May 2015; accepted for publication 1 June 2015; published 29 June 2015)

Purpose: To investigate the feasibility of detecting breast microcalcification (μCa) with a dedicated breast computed tomography (CT) system based on energy-resolved photon-counting silicon (Si) strip detectors.

Methods: The proposed photon-counting breast CT system and a bench-top prototype photon-counting breast CT system were simulated using a simulation package written in MATLAB to determine the smallest detectable μCa. A 14 cm diameter cylindrical phantom made of breast tissue with 20% glandularity was used to simulate an average-sized breast. Five different size groups of calcium carbonate grains, from 100 to 180 μm in diameter, were simulated inside of the cylindrical phantom. The images were acquired with a mean glandular dose (MGD) in the range of 0.7–8 mGy. A total of 400 images was used to perform a reader study. Another simulation study was performed using a 1.6 cm diameter cylindrical phantom to validate the experimental results from a bench-top prototype breast CT system. In the experimental study, a bench-top prototype CT system was constructed using a tungsten anode x-ray source and a single line 256-pixels Si strip photon-counting detector with a pixel pitch of 100 μm. Calcium carbonate grains, with diameter in the range of 105–215 μm, were embedded in a cylindrical plastic resin phantom to simulate μCas. The physical phantoms were imaged at 65 kVp with an entrance exposure in the range of 0.6–8 mGy. A total of 500 images was used to perform another reader study. The images were displayed in random order to three blinded observers, who were asked to give a 4-point confidence rating on each image regarding the presence of μCa. The μCa detectability for each image was evaluated by using the average area under the receiver operating characteristic curve (AUC) across the readers.

Results: The simulation results using a 14 cm diameter breast phantom showed that the proposed photon-counting breast CT system can achieve high detection accuracy with an average AUC greater than 0.89 ± 0.07 for μCas larger than 120 μm in diameter at a MGD of 3 mGy. The experimental results using a 1.6 cm diameter breast phantom showed that the prototype system can achieve an average AUC greater than 0.98 ± 0.01 for μCas larger than 140 μm in diameter using an entrance exposure of 1.2 mGy.

Conclusions: The proposed photon-counting breast CT system based on a Si strip detector can potentially offer superior image quality to detect μCa with a lower dose level than a standard two-view mammography. [http://dx.doi.org/10.1118/1.4922680]

Key words: photon-counting breast CT, microcalcification, detectability, Si strip

1. INTRODUCTION

Breast cancer is the most common cancer and the second major cause of cancer mortality in women.[1] Early and reliable detection of breast cancer can potentially reduce the mortality rate.[2] So far, various x-ray imaging techniques have been investigated for the early detection of breast cancer including two-dimensional (2D) mammography,[3–6] which is the most common imaging technique for screening, and three-dimensional (3D) methods, such as digital breast tomosynthesis[7,8] and dedicated breast cone beam computed tomography (CBCT).[9–11] Digital breast tomosynthesis and CBCT have been developed to solve the problem caused by overlapping anatomical structures in 2D mammography. However, there are still some challenges with digital breast tomosynthesis and CBCT when considering them for the complete replacement of screening mammography. For digital breast tomosynthesis, the broad slice sensitivity profile limits the resolvability of overlapped breast anatomy.[12] CBCT has shown significant improvement in visualization of soft tissue lesions as compared to mammography.[2,10] However, existing CBCT systems based on flat-panel charge-integrating detectors are

limited in their ability to detect microcalcification (μCa) at a clinically relevant radiation dose. A recent report shows that μCa of 150 μm was detectable at a mean glandular dose (MGD) of 10.8 mGy with a high pitch, thick CsI scintillator based CMOS detector.[11]

It is important that breast imaging includes full 3D imaging with high contrast and spatial resolution to detect both soft tissue lesions and μCa. The desired image quality should be achievable with a MGD equal to or less than the dose for the American college of radiology (ACR) phantom using the automatic exposure control (AEC) settings, which is limited by mammography quality standards act (MQSA) to the equivalent of an AGD of 3 mGy per view.[13,14] Photon-counting detectors, which can discriminate the incident photon energy based on pulse height with fast readout electronics, have recently made photon-counting breast computed tomography (CT) feasible.[14–16] Energy-resolved photon-counting detector based breast CT has a number of advantages over CBCT using energy-integrating detectors,[16,17] which includes effective elimination of the potential misregistration artifacts between low- and high-energy image acquisitions, elimination of electronic noise by setting the lowest energy threshold above the electronic noise and below the lowest detectable energy x-ray in the beam, and radiation dose reduction based on improved contrast-to-noise ratio (CNR) through application of optimal energy weighting.

A small pixel pitch silicon (Si) strip photon-counting detector with fast application-specific integrated circuits (ASICs) for breast CT has been developed, and we have shown excellent characteristics in regards to spatial resolution, energy resolution, noise properties, and count rate.[18] Si was chosen as the detector material for photon-counting breast CT due to several advantages over high-Z material such as cadmium telluride (CdTe) and cadmium zinc telluride (CdZnTe). The characteristic x-ray from Si has a very low energy; therefore, it can be used to achieve a high count rate by minimizing the charge-sharing effect with small pixel pitch. In addition, Si has higher material quality and charge collection uniformity than high-Z materials. It is important to consider the Si strip detector for detection of μCa since the smallest detectable μCa at the lowest dose is the most important task remaining for the implementation of breast CT to advance the early detection of breast cancer through screening.[19] We propose using a multi-slit, multislice geometry, which uses fore and aft collimators to minimize the detected scatter radiation, producing fan beam geometry in a helical scanning mode that reduces the patient dose by approximately 40%.[20–22]

An analytical computer simulation has been widely used for not only μCa detectability studies[2,23] but also photon-counting breast CT feasibility studies.[16,24] The simulation can explore the feasibility of new ideas or geometrical parameters for optimization while developing imaging systems. Furthermore, simulated lesion studies can have an advantage in observer studies; for instance, the verification procedure of positive findings can be avoided by simulating the lesions also found in normal cases.[23] However, experimental validation is an essential step before drawing conclusions based on simulation results. In this study, a simulation study was performed to investigate μCa detectability in an average-sized breast phantom with the proposed photon-counting breast CT system geometry. In addition, simulation and experimental studies with a bench-top prototype system were done to validate the simulations with experimental results.

The objectives of this study were to investigate μCa detectability using Si strip photon-counting detector based breast CT by using receiver operating characteristic (ROC) analysis as a subjective evaluation of the system. Simulation and physical phantom studies were performed using different sizes of μCa and radiation dose in the observer study.

2. MATERIALS AND METHODS

2.A. Bench-top prototype photon-counting breast CT system based on a Si strip detector

The experimental images were acquired on a bench-top prototype photon-counting breast CT system shown in Fig. 1. A small field of view (FOV) Si strip photon-counting detector prototype (DxRay, Inc., Northridge, CA) designed for breast imaging was used. It demonstrated high output count rates (100×10^6 cps/mm^2), excellent energy resolution (1.7 keV at 22 keV), and a low electronic noise level (<4 keV). The detector consisted of a single line of 256 pixels with a pixel pitch of 100 μm. An edge illumination design with a 5° tilt angle was applied to the 0.5 mm thick and 1.0 cm long Si sensor, which created an effective interaction length of 6 mm and the dimensions of the detector elements were 0.1×0.5 mm^2. The threshold levels of four discriminators per pixel were individually adjustable. Details of the detector characteristics have previously been reported.[18] A tungsten anode x-ray tube with a focal spot size of 0.8 mm (XRB101, Spellman, Hauppauge, NY) was used as the x-ray source. A high precision direct drive rotary motor (Kollmorgen Goldline DDR D062M, Danaher Motion, Wood Dale, IL) generated the rotational mechanism, and the phantoms were placed on top of a platform, which was positioned over the motor. Fore and aft collimators were used to provide fan beam geometry. The slice thickness (0.46 mm) was determined by the 0.5 mm width of the aft collimator and magnification. A magnification of approximately 1.1 was used to minimize focal spot blurring.

2.B. Simulation

Simulation was performed using a software package written in MATLAB to investigate the μCa detectability with a Si strip detector based photon-counting breast CT system. Simulation

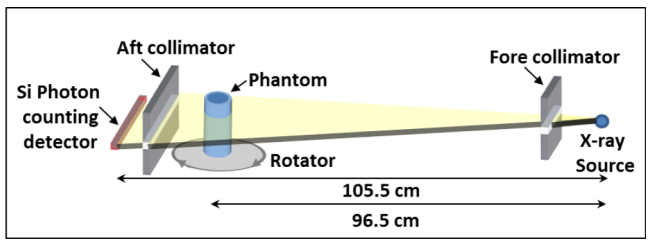

FIG. 1. Schematic diagram of the bench-top prototype photon-counting breast CT system.

TABLE I. Parameters for image acquisition in the simulation studies.

Parameters	Proposed system (for simulation phantom 1)	Prototype system (for simulation phantom 2)
Magnification	1.1	1.1
Tube voltage	65 kVp	65 kVp
Focal spot size	0.3 mm	0.8 mm
Slice thickness	0.1 mm	0.46 mm
Detector thickness	15 mm	6 mm
Number of projections	1229 per rotation	1229 per rotation
Scanning time	25 s per rotation	25 s per rotation
Exposure per rotation	0.7, 1.5, 3, 6, 8 mGy in MGD	1.2, 3, 8 mGy in air kerma

studies were performed using the proposed system specifications shown in Table I for an average-sized breast phantom[25] with a diameter of 14 cm. The specifications of the proposed system such as 0.3 mm focal spot size, 0.1 mm slice thickness, and 15 mm interaction length were determined to optimize the proposed system and maximize its detectability of the μCa and soft tissue lesions. The simulated parameters for the proposed and the bench-top prototype systems are listed in Table I. Electronic noise was not included due to the nature of photon-counting detectors, but Poisson noise was included. Focal spot blurring and beam hardening effects were included, but x-ray scatter effects were not included because good fan beam geometry and scatter rejection by fore and aft collimators were assumed.

2.B.1. Simulation studies for the proposed clinical system

A 14 cm diameter cylindrical phantom (simulation phantom 1) made of breast tissue with 20% glandularity was used to simulate an average-sized female breast [Fig. 2(a)]. Five μCas with diameters of 100, 120, 140, 160, and 180 μm were simulated with calcium carbonate. The simulation was designed to generate randomly patterned clusters of μCas in random locations within 16 regions-of-interest (ROIs). The 16 ROIs were positioned about 27 mm away from the isocenter. Multiple ROIs within one image helped to minimize the simulation time with the assumption that the image quality difference between the ROIs is expected to be negligible due to the uniform background and similar distance from the isocenter. It was also assumed that the image quality would be equivalent whether one or 16 clusters of μCa per phantom are simulated. The images were reconstructed using a filtered back projection (FBP) algorithm with a ramp filter and a voxel size of $23 \times 23 \times 23$ μm^3. To simulate clinical conditions, each image area was magnified, and the extracted ROI was investigated by the observers. Figure 3 shows representative samples of the extracted ROIs from reconstructed images, including five different μCa size groups. A total of 80 extracted ROIs was considered as possible areas of μCa with only half of them including clusters of μCas. Five different dose levels corresponding to a MGD of 0.7, 1.5, 3, 6, and 8 mGy were used. The x-ray exposure was computed in milliroentgens (mR) and converted to air kerma (mGy) by the conversion coefficients (1 R = 8.7 mGy). The MGD was estimated using

$$D_{MG} = D_g N_{CT} \times AK, \quad (1)$$

where D_{MG} is the mean glandular tissue dose (mGy), AK is the air kerma at the isocenter (mGy), and $D_g N_{CT}$ is the normalized glandular dose conversion coefficient (mGy/mGy).[25] Two hundred μCa images (5 sizes of μCas × 5 doses × 8 images for each setting) were combined with 200 control images without μCa to ultimately form 400 images for the observer study.

2.B.2. Simulation studies for the bench-top prototype system

A simulation study (simulation phantom 2) was performed using the exact dimensions of the small physical phantom to validate the simulation software (see Table I). The simulation phantom was generated using polymethyl methacrylate (PMMA) as the base material and μCas with diameter in the range of 100–180 μm [Fig. 2(b)]. The simulation phantom images were generated using entrance skin air kermas (ESAKs) of 1.2, 3, and 8 mGy. The exposure levels for the 1.6 cm phantom (simulation phantom 2) were determined by matching their reconstructed image noise to the noise level in the 14 cm phantom (simulation phantom 1) with MGD in the range of 0.7–8 mGy. The normalized standard deviations for the simulation phantom 2 images were 0.77–1.2 for the ESAK range considered. The normalized standard deviations for the simulation phantom 1 images were 0.8–1.2 for the MGD range considered. Therefore, the noise levels for the small phantom images can represent that in a large phantom. This is due to the fact that the contrast-to-noise ratio of the images is an important factor determining the detectability of μCa. Furthermore, the partial volume effect on the μCa detectability was investigated by varying the slice thickness from 0.1 to 0.46 mm.

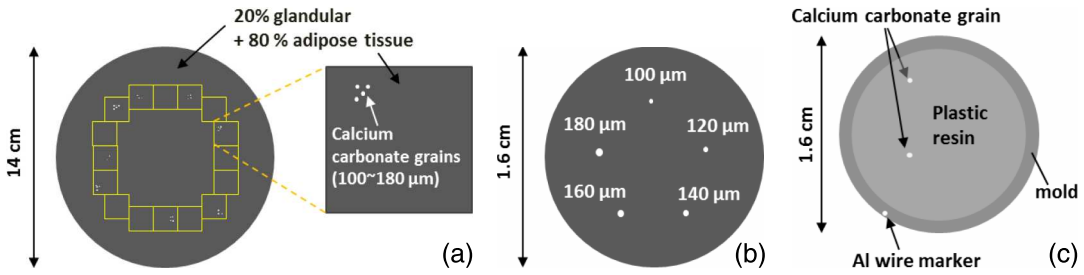

FIG. 2. Schematic diagrams of (a) the simulation phantom 1 with 16 ROIs and extracted ROI for observer study, (b) the simulation phantom 2, and (c) the physical phantom.

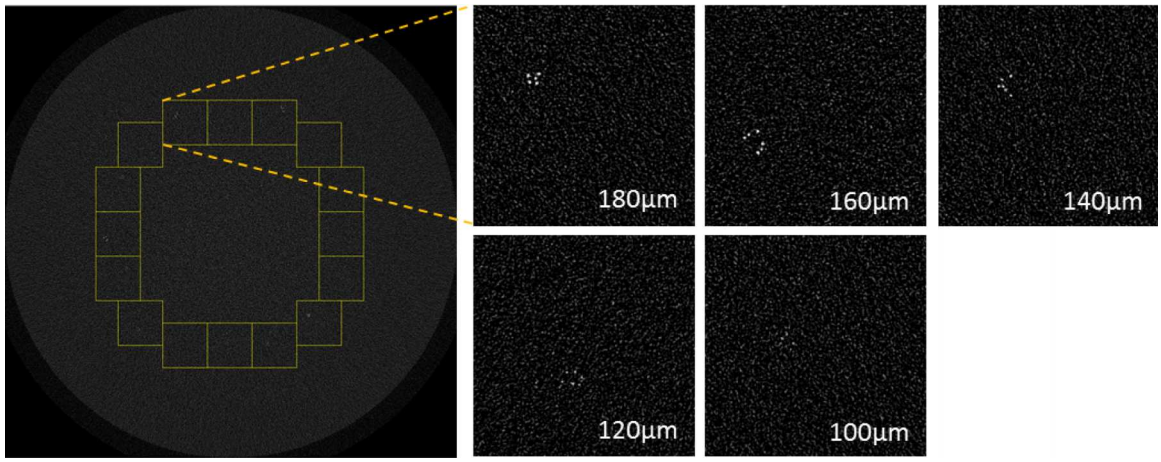

FIG. 3. The reconstructed images of simulation phantom 1 with MGD of 6 mGy. Extracted ROIs from reconstructed images including randomly distributed five different μCa size groups. All ROI images have the same window and level.

2.C. Experimental studies for the bench-top prototype system

A physical phantom was constructed using plastic resin and calcium carbonate (Thermo Fisher Scientific, New Jersey) grains to mimic μCas in a uniform background [Fig. 2(c)]. Various sizes of mesh were used to filter calcium carbonate grains in different size ranges. Calcium carbonate grains of five different diameter ranges of 105–125, 125–140, 140–160, 160–185, and 185–215 μm were embedded in plastic resin. Ten μCa physical phantoms were constructed for each size group. Each physical phantom included one to three calcium carbonate grains. Figure 4 shows representative samples of reconstructed physical phantom images, including five different sizes of μCas.

The x-ray tube voltage was set to 65 kVp and a 2.7 mm aluminum (Al) filter was used yielding a half value layer (HVL) of 2.18 mm Al, which is of reasonable beam quality for dedicated breast CT.[14,26] The electronic noise was eliminated without any loss of signal by setting the noise floor to 4 keV. The rotation speed of the motor was approximately 0.976 rpm, resulting in 1229 frames per scan at 20 frames per second. The images were acquired at five different entrance exposures corresponding to ESAKs of 0.6, 1.2, 3, 6, and 8 mGy per CT scan. The exposure levels were determined by matching the reconstructed image noise levels with respect to the noise levels in simulated 14 cm phantom images with different MGD levels. Different exposure levels were achieved by changing the x-ray tube current. A calibrated ionization chamber (20×6-0.6, Radcal, Monrovia, CA) was used to measure the entrance exposure to the phantom in air kerma (mGy). The middle of the ion chamber was positioned at the same level as the center of fore collimator aperture. The radiation field size was calculated to be larger than the active volume

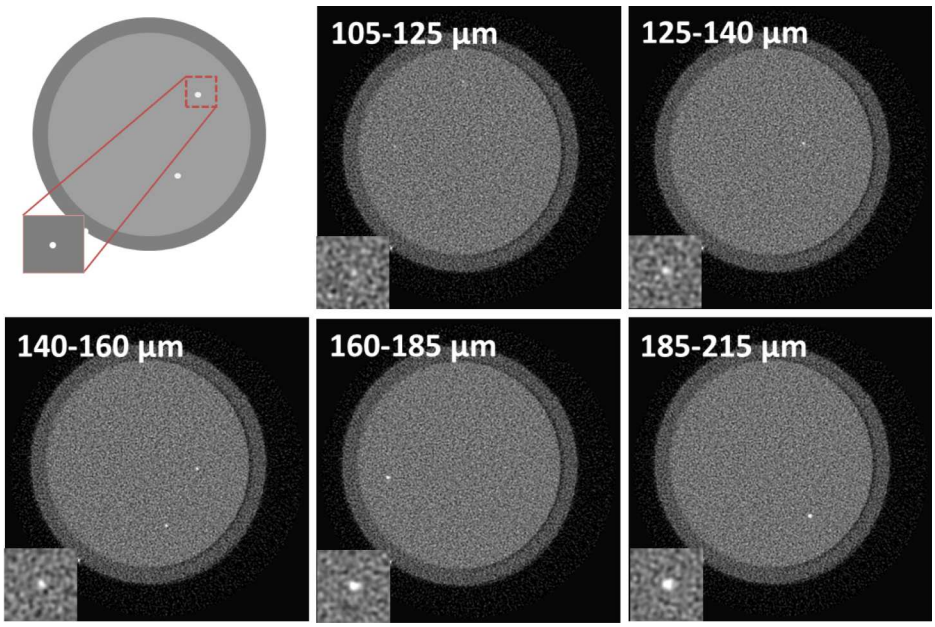

FIG. 4. The reconstructed images of five different size μCas in physical phantoms. The images were acquired as reference images with ESAK of 8 mGy. The lower left corner of each image shows the extracted area with μCa. All images have the same window and level.

of the ion chamber at the isocenter. The sensitivity variation across the pixels was compensated by implementing a flat-field correction technique, which used open flood field images. The images were reconstructed by using a FBP algorithm with a ramp filter and a voxel size of $23\times23\times23$ μm^3. Two hundred fifty μCa images (5 sizes of μCas × 5 doses ×10 images for each setting) were combined with 250 control images without μCa to ultimately form 500 images for the observer study.

2.D. Observer study

An observer study was conducted to evaluate the μCa detectability for various combinations of μCa sizes and dose levels. The images were displayed to three observers in random order. In order to familiarize the observers with the setup and images, 50 simulations and 75 experimental reconstructed images were used for a training session, which was administered prior to the study. Observers were allowed to adjust the window width, level, and magnification of the images for optimal visualization. Observers were asked to rate the presence of a μCa using a 4-point confidence-rating defined as 1—definitely absent, 2—probably absent, 3—probably present, and 4—definitely present.

A multireader, multicase (MRMC) ROC program version 2.4 (University of Iowa) was used to analyze the data.[27] The area under the ROC curve (AUC) was calculated using the "trapezoidal/Wilcoxon" curve fitting option in the program, which is an empirical AUC estimation method. The empirical true and false positive fractions were calculated using

$$\mathrm{TPF}(r) = \frac{1}{n_T}\sum_{i=1}^{n_T} I[X_i \geq r], \tag{2}$$

$$\mathrm{FPF}(r) = \frac{1}{n_F}\sum_{j=1}^{n_F} I[Y_j \geq r], \tag{3}$$

where r is each distinct rating, X_i, $i = 1,\ldots,n_T$ are the μCa included image ratings, and Y_j, $j = 1,\ldots,n_F$ are the normal image ratings. The indicator function, $I[\cdot]$, assigned 1 or 0 if the result was true or false, respectively. The AUC was calculated by sum of the trapezoid areas under the linearly connected points.[28] Statistical analysis was performed by using a fixed readers and random cases analysis within the Obuchowski–Rockette (OR) analysis[29,30] with a jackknife covariance estimation framework. The averaged AUC across readers was used to compare μCa detection accuracy for various sizes and radiation doses.

3. RESULTS

3.A. Simulation

3.A.1. Simulation results for the proposed clinical system

Figure 5 shows the magnified regions containing five different sizes of μCas in the reconstructed images at different radiation doses for a 14 cm phantom. Nearly, all sizes of μCas in each cluster were detectable with a MGD of 3 mGy, except for 100 μm. It was possible to detect 140, 160, and 180 μm μCas with a MGD of 1.5 mGy; however, some μCas became increasingly difficult to detect as size decreases. With the exception of μCas larger than 160 μm, it was difficult to detect μCas with a MGD of 0.7 mGy. The averaged AUC for various μCa sizes as a function of the MGD is shown in Fig. 6. Additionally, the limits of the smallest detectable μCa for different MGD levels are shown. Higher AUC represents higher accuracy of the μCa detectability. The AUC gradually decreased with decreasing μCa size and MGD. The average AUC for almost all μCa sizes, with the exception of 100 μm μCa, was higher than 0.89 ± 0.07 at a MGD of 3 mGy. The average AUC for 160–180 μm μCas was greater than 0.78 ± 0.04 for all dose ranges tested. Table II lists the mean AUC differences, z-test statistic, p-values, and 95% confidence intervals only if AUC differences between different sizes of μCa were significant. The difference of AUC was considered significant when p-value was less than 0.05. The detectability of 120 μm μCas showed no significant difference as compared with larger size μCas at a MGD of 3 mGy. In addition, μCas in size ranges of 140–180 and 160–180 μm have significantly higher detection accuracy than smaller μCa sizes at MGD of 1.5 and 0.7 mGy, respectively.

3.A.2. Simulation results for the bench-top prototype system

Figure 7(a) shows the reconstructed simulation phantom images with slice thickness of 0.46 mm, which was the same as the bench-top prototype system. The μCas below 140 μm were difficult to detect with 3 mGy of ESAK. Figure 7(b) shows the reconstructed images with slice thickness of 0.1 mm. The μCas below 140 μm could be detected even with 1.2 mGy of ESAK. The results show that the visibility of μCas below 140 μm at a low dose could be improved by using a 0.1 mm slice thickness.

3.B. Experimental results using the bench-top prototype system

Figure 8 shows magnified areas of five different sizes of μCas at various ESAKs. The three size groups of μCas larger than 140 μm were clearly detectable with well-preserved shape at ESAK of 3 mGy; however, with ESAK of 1.2 mGy, these three size groups were still detectable, but the shape was deformed. μCas smaller than 140 μm were only clearly detectable with an ESAK of at least 6 mGy. Additionally, they were difficult to differentiate from quantum noise for ESAK of 3 mGy, which is in agreement with the simulation results shown in Fig. 7(a). Only μCas in the range of 185–215 μm were clearly detectable for the entire ESAK range of 0.6–8 mGy. The average AUC for various μCa sizes as a function of the ESAK are shown in Fig. 9. The prototype system showed an average AUC greater than 0.83 ± 0.05 and 0.98 ± 0.01 for the μCas larger than 140 μm at ESAKs of 0.6 and 1.2 mGy, respectively. However, for μCas smaller than 140 μm with an ESAK below 3 mGy, the average AUC decreased to less than 0.83, which is in agreement with simulation results in Fig. 7(a). Table III lists the mean AUC differences, z-test statistic,

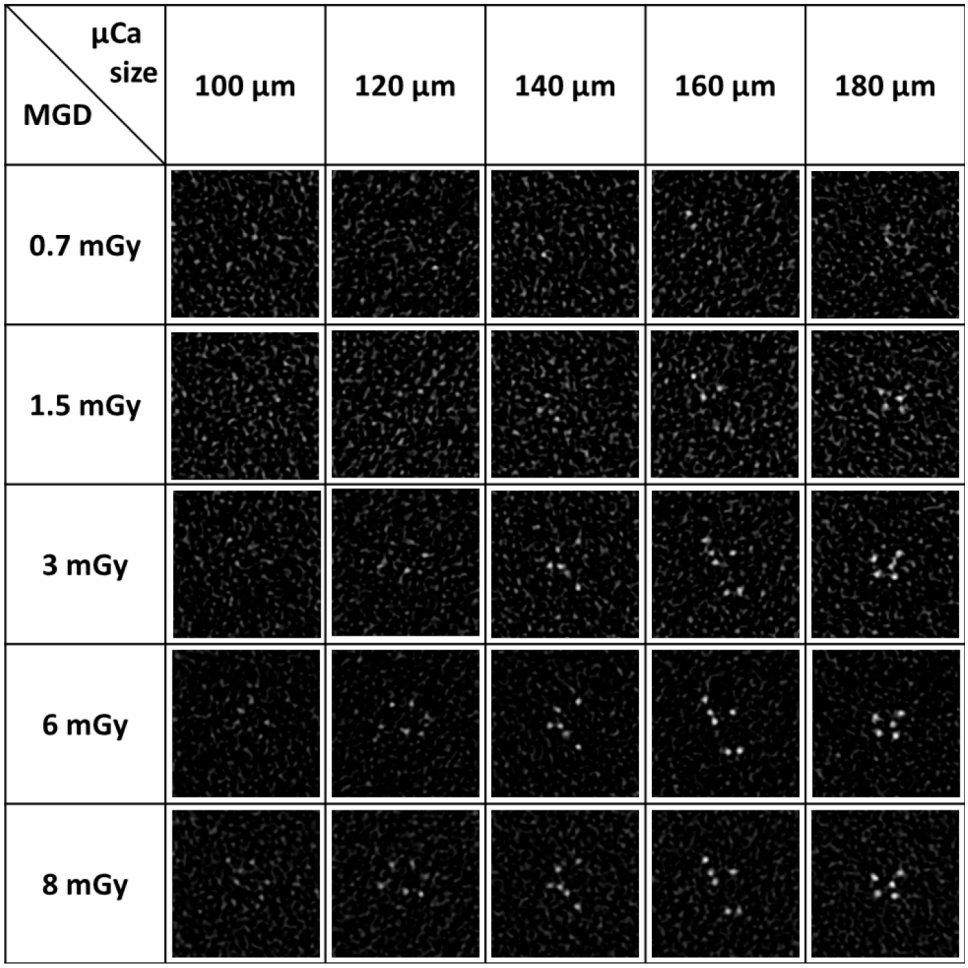

FIG. 5. Magnified areas with μCas are shown in the reconstructed images of simulation phantom 1 including five different sizes of μCas. Each column shows the same μCa cluster with different MGDs. All images have the same window and level.

p-values, and 95% confidence intervals only if AUC differences between different sizes of μCa were significant. The AUC differences in the ranges of 105–140 and 140–215 μm were not significant for the ESAK range of 0.6–8 mGy.

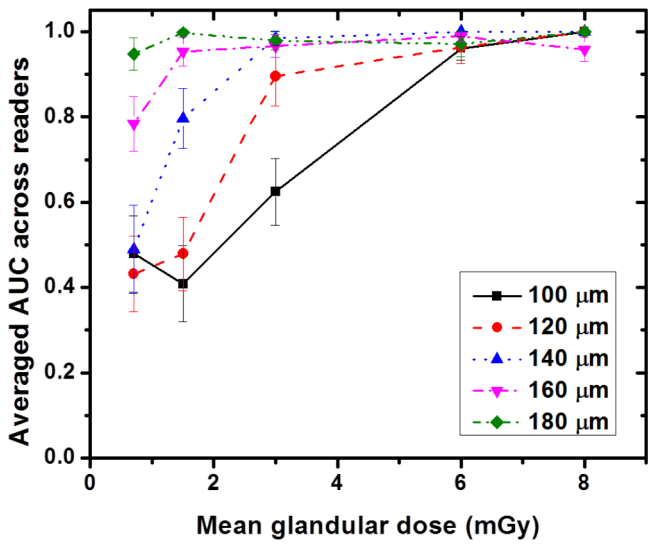

FIG. 6. The average AUC for various μCa sizes as a function of MGD with error bars indicating the standard deviation among three observers.

Conversely, the AUCs of μCas in the range of 105–140 μm were significantly different from larger μCas at an ESAK lower than 3 mGy.

4. DISCUSSION

Several volumetric breast imaging techniques have been developed to address the limitation of screening mammography in lesion detection due to anatomical noise, especially in dense breasts.[8,9,31] However, the detection of μCas, which is an important marker for breast cancer,[32,33] is still limited by spatial resolution and radiation dose in previously reported volumetric imaging systems.[2,11] The recent development of energy-resolved photon-counting detectors that count and separate individual photons according to their energies demonstrate that low noise and high contrast images can be acquired with low dose.[16,34] A previously reported bench-top prototype of photon-counting breast CT system[18] was evaluated for detectability of μCa using different radiation doses.

The detectability of μCas in an average-sized breast phantom was simulated based on the proposed photon-counting breast CT system. Irregular patterns and random distribution of μCas were simulated as clusters in the phantoms to create

TABLE II. Confidence intervals of 95% for treatment AUC differences in the simulation results where treatments 1–5 correspond to 100, 120, 140, 160, and 180 μm, respectively. Z: z-test statistic, CI: confidence interval.

MGD	Treatment comparison	Treatment AUC difference	Standard error	Z	Pr > |z|	95% CI
3 mGy	1–2	−0.270 83	0.067 22	−4.03	0.0001	(−0.402 59, −0.139 08)
	1–3	−0.359 38	0.067 22	−5.35	0.0000	(−0.491 13, −0.227 62)
	1–4	−0.341 15	0.067 22	−5.07	0.0000	(−0.472 90, −0.209 39)
	1–5	−0.354 17	0.067 22	−5.27	0.0000	(−0.485 92, −0.222 41)
1.5 mGy	1–3	−0.388 02	0.094 77	−4.09	0.0000	(−0.573 77, −0.202 28)
	1–4	−0.544 27	0.094 77	−5.74	0.0000	(−0.730 02, −0.358 53)
	1–5	−0.588 54	0.094 77	−6.21	0.0000	(−0.774 29, −0.358 53)
	2–3	−0.317 71	0.094 77	−3.35	0.0008	(−0.503 45, −0.131 96)
	2–4	−0.473 96	0.094 77	−5	0.0000	(−0.659 70, −0.288 21)
	2–5	−0.518 23	0.094 77	−5.47	0.0000	(−0.703 97, −0.332 48)
0.7 mGy	1–4	−0.304 69	0.102 18	−2.98	0.0029	(−0.504 95, −0.104 43)
	1–5	−0.468 75	0.102 18	−4.59	0.0000	(−0.669 01, −0.268 49)
	2–4	−0.351 56	0.102 18	−3.44	0.0006	(−0.551 82, −0.151 30)
	2–5	−0.515 62	0.102 18	−5.05	0.0000	(−0.715 89, −0.315 36)
	3–4	−0.294 27	0.102 18	−2.88	0.0040	(−0.494 53, −0.094 01)
	3–5	−0.458 33	0.102 18	−4.49	0.0000	(−0.658 59, −0.258 07)

more realistic lesions.[35] In this study, various sizes of spherical μCas were simulated to determine the smallest detectable μCa at different radiation doses, even though morphological shapes of μCa include irregular forms or linear structures.[36] A previous report using cone beam breast CT with a high pitch, thick CsI scintillator based CMOS detector has shown that 150 μm μCas could be detected at a MGD of 10.8 mGy.[11] Another simulation study using spiral breast CT with a CdTe based photon-counting detector predicted that 150 μm μCas could be detected at a MGD of 3 mGy.[14] Our results indicate that the proposed photon-counting breast CT system has an AUC greater than 0.89 ± 0.07 for μCas larger than 120 μm at a MGD of 3 mGy. Our results also indicate that μCas in the range of 140–160 μm were detectable with a MGD of 1.5 mGy.

We designed simulation and experimental studies with the bench-top prototype photon-counting breast CT system to validate the simulation results for the proposed clinical breast CT system. The agreement between simulation and experiment for the small phantoms imaged with the bench-top prototype breast CT system indicates that the proposed clinical breast CT system will have similar results because the main scanning geometry and the image noise level will be comparable. The smallest detectable μCa size from simulation was compared with the experimental results using the bench-top prototype breast CT system. Both simulation and experimental

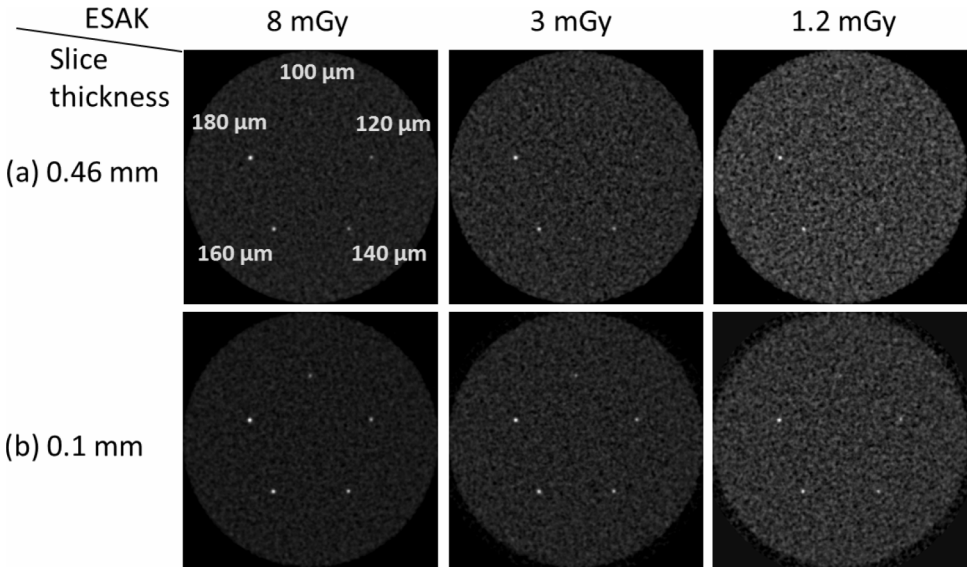

FIG. 7. The reconstructed images of simulation phantom 2 with (a) slice thickness of 0.46 mm with (b) slice thickness of 0.1 mm. All images have the same window and level.

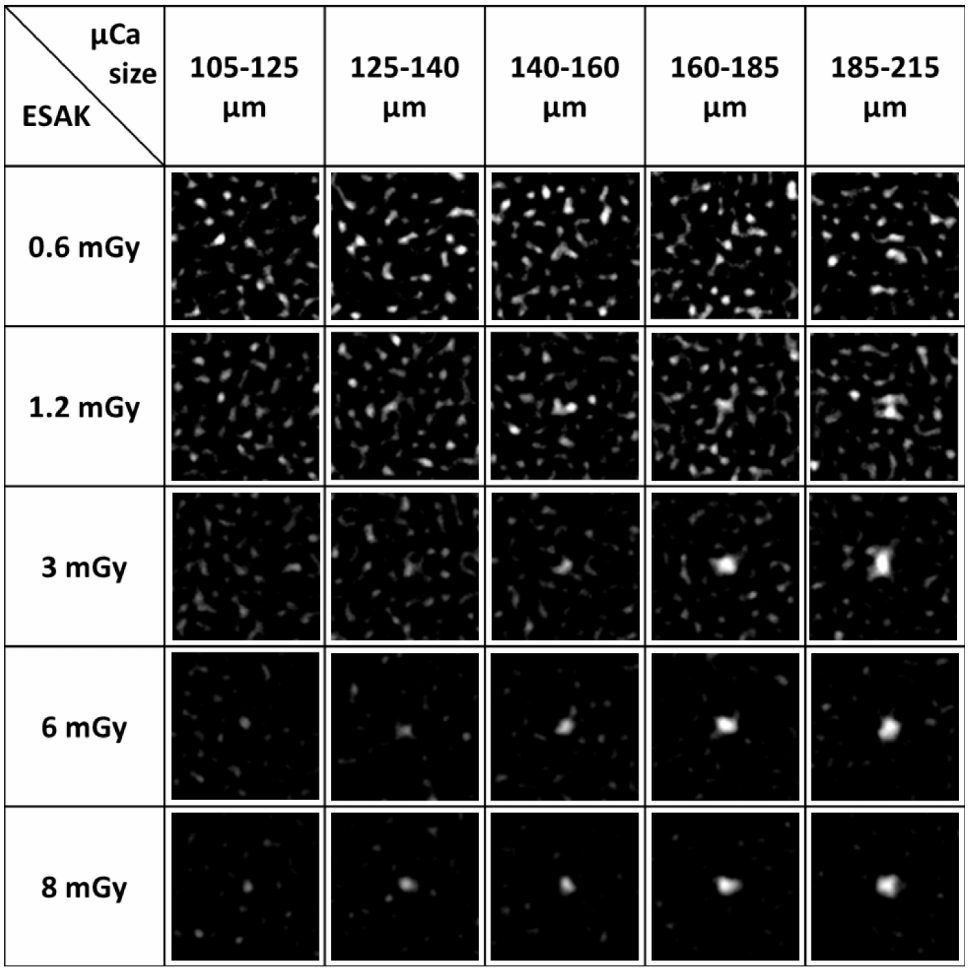

FIG. 8. Magnified areas with μCa are shown in the reconstructed images of the physical phantom including five different sizes μCa. Each column shows the same μCa with different ESAK. All images have the same window and level.

results show that μCas smaller than 140 μm were gradually more difficult to differentiate from the background noise with lower ESAK than 3 mGy. The size and contrast of μCas in a range of 125–140 μm at an ESAK of 3 mGy were similar to the background noise. Also, experimental observer study results showed a notable drop in AUC for μCas smaller than 140 μm using an ESAK of 3 mGy. This μCa detectability was lower than the simulation results with the proposed photon-counting breast CT system, which showed good detectability for 140 μm μCas with low dose. Simulation studies with the prototype breast CT system were also performed using 0.1 mm slice thickness assuming that the difference in slice thickness was the major cause for the reduction in μCa detectability. A simulation study on various slice thicknesses demonstrated that the detectability of μCas smaller than 140 μm can be improved with reducing the slice thickness. The theoretical potential of the detector based on 10% of modulation transfer function, 5.4 mm^{-1},[18] can be realized in lesion detection by reducing the slice thickness to minimize the partial volume effect.

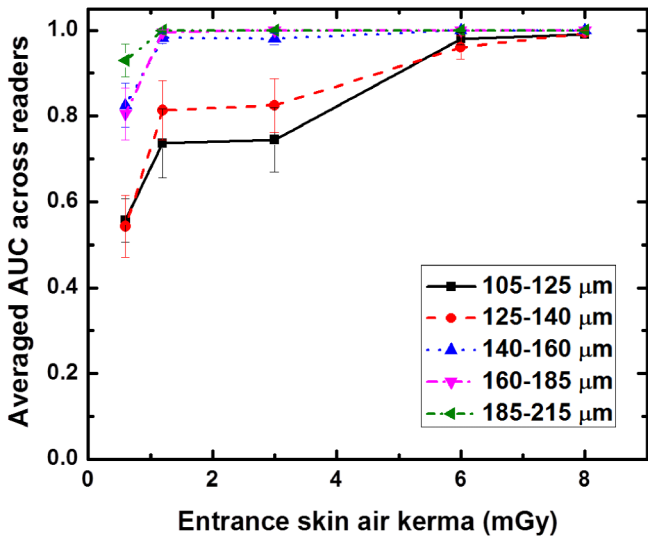

FIG. 9. The average AUC for different μCa sizes as a function of the ESAK, where error bars indicate the standard deviation among the three observers.

The eventual clinical implementation will be a multislit, multislice geometry design, which has previously been implemented in projection x-ray imaging.[20,37,38] The detectors will be mounted with a gap of 4 mm between adjacent detector slices. A total of 49 detector slices will be enough to cover a FOV of 16 cm at the isocenter with the given magnification. The gap between each detector slice will be covered using a helical scanning mode with a pitch of 2 for a linear travel

TABLE III. Confidence intervals of 95% for treatment AUC differences in the experimental results where treatments 1–5 correspond to 105–125, 125–140, 140–160, 160–185, 185–215 μm, respectively. Z: z-test statistic, CI: confidence interval.

MGD	Treatment comparison	Treatment AUC difference	Standard error	Z	Pr > |z|	95% CI
3 mGy	1–3	−0.235	0.064 47	−3.65	0.0003	(−0.361 35, −0.108 65)
	1–4	−0.255	0.064 47	−3.96	0.0001	(−0.381 35, −0.128 65)
	1–5	−0.255	0.064 47	−3.96	0.0001	(−0.381 35, −0.128 65)
	2–3	−0.155	0.064 47	−2.40	0.0162	(−0.281 35, −0.028 65)
	2–4	−0.175	0.064 47	−2.71	0.0066	(−0.301 35, −0.048 65)
	2–5	−0.175	0.064 47	−2.71	0.0066	(−0.301 35, −0.048 65)
1.2 mGy	1–3	−0.245	0.065 29	−3.75	0.0002	(−0.372 97, −0.117 03)
	1–4	−0.258	0.065 29	−3.96	0.0001	(−0.386 30, −0.130 37)
	1–5	−0.263	0.065 29	−4.03	0.0001	(−0.391 30, −0.135 37)
	2–3	−0.150	0.065 29	−2.30	0.0216	(−0.277 97, −0.022 03)
	2–4	−0.163	0.065 29	−2.50	0.0124	(−0.291 30, −0.035 37)
	2–5	−0.168	0.065 29	−2.58	0.0099	(−0.296 30, −0.040 37)
0.6 mGy	1–3	−0.268	0.081 81	−3.28	0.0010	(−0.428 67, −0.108 00)
	1–4	−0.248	0.081 81	−3.04	0.0024	(−0.408 67, −0.088 00)
	1–5	−0.373	0.081 81	−4.56	0.0000	(−0.533 67, −0.213 00)
	2–3	−0.282	0.081 81	−3.44	0.0006	(−0.442 00, −0.121 33)
	2–4	−0.262	0.081 81	−3.20	0.0014	(−0.422 00, −0.101 33)
	2–5	−0.387	0.081 81	−4.73	0.0000	(−0.547 00, −0.226 33)

equivalent to the detector slice gap. Therefore, the actual number of scans per detector slice will be 20.

While the study investigated potential improvement of μCa detectability with Si strip photon-counting breast CT, there were several limitations. First, the uniform background material can improve detectability of μCa as compared to the anatomical background structure; however, the most initial feasibility studies of μCa detectability in new imaging systems were performed with uniform background phantoms.[2,11,14,39] A uniform background material should be acceptable because this study investigated the smallest detectable μCa and finding an optimal geometrical strategy to improve the results.

Second, the size of the calcium carbonate grains used for the physical phantom could not be uniformly distributed within a size range. The experimental results of the ROC curve show a sudden reduction in AUC for 125–140 μm μCas at an ESAK of 3 mGy, which is different from simulation results that showed a gradual reduction in AUC. The actual grain sizes in the ranges of 125–140 and 140–160 μm may have been closer to 125 and 160 μm, respectively.

Third, the spectral information was not utilized to improve object contrast, such as an optimal energy weighting technique.[40] The optimal energy weighting technique can improve the CNR of the target by giving higher weight to lower energy photons.[16,24,41] Previous studies have shown maximum CNR improvement of about 5.2% and 9% by applying optimal energy weighting for μCas in size range of 50–500 μm with mammography using Si strip and ideal photon-counting detectors, respectively.[41–43] A recent simulation study with a CZT based photon-counting detector for breast CT has reported a 19% higher AUC for the detection of 240 μm μCa, which was achieved by using an energy weighting technique as compared to a charge-integrating detector.[23] The detectability of μCa could potentially be improved if spectral information is optimally utilized in future studies, although the CNR improvement from energy weighting will depend on the detector efficiency and input spectra.[3,23]

5. CONCLUSIONS

The results indicate that a photon-counting breast CT system based on a Si strip detector with multislit geometry can offer superior image quality to detect μCas with a lower dose level than a charge-integrating flat-panel detector based CBCT. Furthermore, the proposed photon-counting breast CT system is expected to offer superior image quality to detect μCa with a radiation dose lower than a standard two-view mammography.

ACKNOWLEDGMENT

This work was supported in part by NIH/NCI Grant No. R01CA13687.

[a]Present address: Center for Medical Metrology, Koreas Research Institute of Standards and Science, Daejeon, Korea.
[b]Author to whom correspondence should be addressed. Electronic mail: symolloi@uci.edu; Telephone: (949) 824-5904; Fax: (949) 824-8115.

[1]R. Siegel, J. Ma, Z. Zou, and A. Jemal, "Cancer statistics, 2014," Ca-Cancer J. Clin. **64**, 9–29 (2014).
[2]C.-J. Lai, C. C. Shaw, L. Chen, M. C. Altunbas, X. Liu, T. Han, T. Wang, W. T. Yang, G. J. Whitman, and S.-J. Tu, "Visibility of microcalcification in cone beam breast CT: Effects of x-ray tube voltage and radiation dose," Med. Phys. **34**, 2995–3004 (2007).

[3]L. Desponds, C. Depeursinge, M. Grecescu, C. Hessler, A. Samiri, and J. Valley, "Influence of anode and filter material on image quality and glandular dose for screen-film mammography," Phys. Med. Biol. **36**, 1165–1182 (1991).
[4]C. J. D'Orsi, "Early detection of breast cancer: Mammography," Breast Cancer Res. Treat. **18**, S107–S109 (1991).
[5]K. Pinker, N. Perry, S. Milner, K. Mokbel, and S. Duffy, "Accuracy of breast cancer detection with full-field digital mammography and integral computer-aided detection correlated with breast density as assessed by a new automated volumetric breast density measurement system," Breast Cancer Res. **12**, P4 (2010).
[6]C. K. Kuhl, S. Schrading, C. C. Leutner, N. Morakkabati-Spitz, E. Wardelmann, R. Fimmers, W. Kuhn, and H. H. Schild, "Mammography, breast ultrasound, and magnetic resonance imaging for surveillance of women at high familial risk for breast cancer," J. Clin. Oncol. **23**, 8469–8476 (2005).
[7]L. T. Niklason, B. T. Christian, L. E. Niklason, D. B. Kopans, D. E. Castleberry, B. Opsahl-Ong, C. E. Landberg, P. J. Slanetz, A. A. Giardino, and R. Moore, "Digital tomosynthesis in breast imaging," Radiology **205**, 399–406 (1997).
[8]J. T. Dobbins III and D. J. Godfrey, "Digital x-ray tomosynthesis: Current state of the art and clinical potential," Phys. Med. Biol. **48**, R65–R106 (2003).
[9]J. M. Boone, T. R. Nelson, K. K. Lindfors, and J. A. Seibert, "Dedicated breast CT: Radiation dose and image quality evaluation1," Radiology **221**, 657–667 (2001).
[10]K. K. Lindfors, J. M. Boone, T. R. Nelson, K. Yang, A. L. Kwan, and D. F. Miller, "Dedicated breast CT: Initial clinical experience," Radiology **246**, 725–733 (2008).
[11]Y. Shen, Y. Zhong, C. J. Lai, T. Wang, and C. C. Shaw, "Cone beam breast CT with a high pitch (75 mum), thick (500 mum) scintillator CMOS flat panel detector: Visibility of simulated microcalcifications," Med. Phys. **40**, 101915 (10pp.) (2013).
[12]A. Nosratieh, K. Yang, S. Aminololama-Shakeri, and J. M. Boone, "Comprehensive assessment of the slice sensitivity profiles in breast tomosynthesis and breast CT," Med. Phys. **39**, 7254–7261 (2012).
[13]American College of Radiology, "ACR practice parameter for the performance of screening and diagnostic mammography," in *American College of Radiology* (American College of Radiology, Reston, VA, 2014).
[14]W. A. Kalender, M. Beister, J. M. Boone, D. Kolditz, S. V. Vollmar, and M. C. Weigel, "High-resolution spiral CT of the breast at very low dose: Concept and feasibility considerations," Eur. Radiol. **22**, 1–8 (2012).
[15]W. C. Barber, E. Nygard, J. C. Wessel, N. Malakhov, G. Wawrzyniak, N. E. Hartsough, T. Gandhi, and J. S. Iwanczyk, "Fast photon counting CdTe detectors for diagnostic clinical CT: Dynamic range, stability, and temporal response," Proc. SPIE **7622**, 76221E (2010).
[16]H. Q. Le, J. L. Ducote, and S. Molloi, "Radiation dose reduction using a CdZnTe-based computed tomography system: Comparison to flat-panel detectors," Med. Phys. **37**, 1225–1236 (2010).
[17]H. Q. Le and S. Molloi, "Segmentation and quantification of materials with energy discriminating computed tomography: A phantom study," Med. Phys. **38**, 228–237 (2011).
[18]H.-M. Cho, W. C. Barber, H. Ding, J. S. Iwanczyk, and S. Molloi, "Characteristic performance evaluation of a photon counting Si strip detector for low dose spectral breast CT imaging," Med. Phys. **41**, 091903 (10pp.) (2014).
[19]G. Hermann, C. Janus, I. S. Schwartz, A. Papatestas, D. G. Hermann, and J. G. Rabinowitz, "Occult malignant breast lesions in 114 patients: Relationship to age and the presence of microcalcifications," Radiology **169**, 321–324 (1988).
[20]M. Åslund, B. Cederström, M. Lundqvist, and M. Danielsson, "Scatter rejection in multislit digital mammography," Med. Phys. **33**, 933–940 (2006).
[21]M. Lundqvist, M. Danielsson, B. Cederstroem, V. Chmill, A. Chuntonov, and M. Aslund, "Measurements on a full-field digital mammography system with a photon counting crystalline silicon detector," Proc. SPIE **5030**, 547–552 (2003).
[22]G. T. Barnes, H. M. Cleare, and I. A. Brezovich, "Reduction of scatter in diagnostic radiology by means of a scanning multiple slit assembly 1," Radiology **120**, 691–694 (1976).
[23]E. Shaheen, C. Van Ongeval, F. Zanca, L. Cockmartin, N. Marshall, J. Jacobs, K. C. Young, D. R. Dance, and H. Bosmans, "The simulation of 3D microcalcification clusters in 2D digital mammography and breast tomosynthesis," Med. Phys. **38**, 6659–6671 (2011).
[24]K. S. Kalluri, M. Mahd, and S. J. Glick, "Investigation of energy weighting using an energy discriminating photon counting detector for breast CT," Med. Phys. **40**, 081923 (16pp.) (2013).
[25]J. Boone, N. Shah, and T. Nelson, "A comprehensive analysis of DgNCT coefficients for pendant-geometry cone-beam breast computed tomography," Med. Phys. **31**, 226–235 (2004).
[26]M. Weigel, S. V. Vollmar, and W. A. Kalender, "Spectral optimization for dedicated breast CT," Med. Phys. **38**, 114–124 (2011).
[27]K. B. C. Metz and D. Dorfman, see http://perception.radiology.uiowa.edu/Software/ReceiverOperatingCharacteristicROC/DBMMRMC/tabid/116/Default.aspx for DBM MRMC.
[28]E. R. DeLong, D. M. DeLong, and D. L. Clarke-Pearson, "Comparing the areas under two or more correlated receiver operating characteristic curves: A nonparametric approach," Biometrics **44**, 837–845 (1988).
[29]N. A. Obuchowski, Jr. and H. E. Rockette, Jr., "Hypothesis testing of diagnostic accuracy for multiple readers and multiple tests an ANOVA approach with dependent observations," Commun. Stat.-Simul. Comput. **24**, 285–308 (1995).
[30]S. L. Hillis, N. A. Obuchowski, K. M. Schartz, and K. S. Berbaum, "A comparison of the Dorfman–Berbaum–Metz and Obuchowski–Rockette methods for receiver operating characteristic (ROC) data," Stat. Med. **24**, 1579–1607 (2005).
[31]J. S. Sung, C. H. Lee, E. A. Morris, K. C. Oeffinger, and D. D. Dershaw, "Screening breast MR imaging in women with a history of chest irradiation," Radiology **259**, 65–71 (2011).
[32]E. Fondrinier, G. Lorimier, V. Guerin-Boblet, A. F. Bertrand, C. Mayras, and N. Dauver, "Breast microcalcifications: Multivariate analysis of radiologic and clinical factors for carcinoma," World J. Surg. **26**, 290–296 (2002).
[33]E. S. Burnside, J. E. Ochsner, K. J. Fowler, J. P. Fine, L. R. Salkowski, D. L. Rubin, and G. A. Sisney, "Use of microcalcification descriptors in BI-RADS 4th edition to stratify risk of malignancy," Radiology **242**, 388–395 (2007).
[34]H. Ding, J. L. Ducote, and S. Molloi, "Breast composition measurement with a cadmium-zinc-telluride based spectral computed tomography system," Med. Phys. **39**, 1289–1297 (2012).
[35]M. Das, H. C. Gifford, J. M. O'Connor, and S. J. Glick, "Evaluation of a variable dose acquisition technique for microcalcification and mass detection in digital breast tomosynthesis," Med. Phys. **36**, 1976–1984 (2009).
[36]F. Zanca, D. P. Chakraborty, C. Van Ongeval, J. Jacobs, F. Claus, G. Marchal, and H. Bosmans, "An improved method for simulating microcalcifications in digital mammograms," Med. Phys. **35**, 4012–4018 (2008).
[37]G. T. Barnes and I. A. Brezovich, "The design and performance of a scanning multiple slit assembly," Med. Phys. **6**, 197–204 (1979).
[38]M. V. Yester, G. T. Barnes, and M. A. King, "Experimental measurements of the scatter reduction obtained in mammography with a scanning multiple slit assembly," Med. Phys. **8**, 158–162 (1981).
[39]X. Gong, A. A. Vedula, and S. J. Glick, "Microcalcification detection using cone-beam CT mammography with a flat-panel imager," Phys. Med. Biol. **49**, 2183–2195 (2004).
[40]M. J. Tapiovaara and R. Wagner, "SNR and DQE analysis of broad spectrum x-ray imaging," Phys. Med. Biol. **30**, 519–529 (1985).
[41]J. Berglund, H. Johansson, M. Lundqvist, B. Cederström, and E. Fredenberg, "Energy weighting improves dose efficiency in clinical practice: Implementation on a spectral photon-counting mammography system," J. Med. Imaging **1**, 031003 (2014).
[42]R. Cahn, B. Cederström, M. Danielsson, A. Hall, M. Lundqvist, and D. Nygren, "Detective quantum efficiency dependence on x-ray energy weighting in mammography," Med. Phys. **26**, 2680–2683 (1999).
[43]J. Giersch, D. Niederlöhner, and G. Anton, "The influence of energy weighting on x-ray imaging quality," Nucl. Instrum. Methods Phys. Res., Sect. A **531**, 68–74 (2004).